methane

MDPI

Review

Modification Strategies of Ni-Based Catalysts with Metal Oxides for Dry Reforming of Methane

Xingyuan Gao [1,2,3], Weihao Lin [1], Zhiyong Ge [1], Hongming Ge [1] and Sibudjing Kawi [3,*]

[1] Department of Chemistry and Material Science, Guangdong University of Education, Guangzhou 510303, China; gaoxingyuan@gdei.edu.cn (X.G.); linweihao@gdei.edu.cn (W.L.); gezhiyong@gdei.edu.cn (Z.G.); gehongming@gdei.edu.cn (H.G.)
[2] Engineering Technology Development Center of Advanced Materials and Energy Saving and Emission Reduction in Guangdong Colleges and Universities, Guangzhou 510303, China
[3] Department of Chemical and Biomolecular Engineering, National University of Singapore, Singapore 117585, Singapore
* Correspondence: chekawis@nus.edu.sg; Tel.: +65-6516-6312

Abstract: Syngas generated from the catalytic dry reforming of methane (DRM) enables the downstream production of H_2 fuel and value-added chemicals. Ni-based catalysts with metal oxides, as both supports and promoters, are widely applied in the DRM reaction. In this review, four types of metal oxides with support confinement effect, metal-support interaction, oxygen defects, and surface acidity/basicity are introduced based on their impacts on the activity, selectivity, and stability of the Ni-based catalyst. Moreover, the structure–performance relationships are discussed in-depth. Finally, conclusive remarks and prospects are proposed.

Keywords: Ni catalyst; metal oxide; dry reforming of methane; syngas

Citation: Gao, X.; Lin, W.; Ge, Z.; Ge, H.; Kawi, S. Modification Strategies of Ni-Based Catalysts with Metal Oxides for Dry Reforming of Methane. *Methane* **2022**, *1*, 139–157. https://doi.org/10.3390/methane1030012

Academic Editor: Mateusz Wnukowski

Received: 7 April 2022
Accepted: 2 June 2022
Published: 21 June 2022

1. Introduction

CO_2 and CH_4 are two main sources of greenhouse gases released from industry and human activities, which adversely influences the natural environment and biological diversity [1–4]. A promising strategy to address the above issues is conversion of both gases into valuable products, such as syngas—a mixture of CO and H_2, which can be further transformed into pure H_2 via separation membranes or value-added chemicals (e.g., acetic acid, methanol, oxyalcohol, dimethyl ether, and long-chain hydrocarbons) via combination reactions [5–10].

Due to the strong endothermic forward reaction, a high temperature (600–800 °C) is usually needed to activate the reactant molecules. The utilization of catalysts certainly lowers the activation barrier and changes the reaction pathway. Noble metals exhibit a high conversion and anti-coking property; however, the limited reserve and high cost hinder their large-scale applications. In comparison, Ni-based catalysts are low cost and comparable catalytic activities, thus presenting a competitive application potential in the DRM reaction [11–13]; however, owing to the intensive reaction conditions, metal sintering is more likely to occur than in mild conditions, resulting in a loss of surface area and an activity drop. Additionally, coke formation from CH_4 decomposition and CO disproportionation easily covers the active sites and blocks the reactor [14–17]; therefore, modifications are necessary to develop a highly active and robust Ni-based catalyst.

Since CO_2 can be adsorbed and activated at the metal and oxygen ions, metal oxides (e.g., basic oxides, rare earth metal oxides, transition metal oxides, and mixed oxides) with oxygen defects and surface basicity are widely applied as supports or promoters [18–22]. In particular, strong basicity enhances the CO_2 conversion efficiency and facilitates the dissociation of CO_2 into CO and O radicals, leading to immediate carbon removal [23–25]. On the other hand, the existence of oxygen defects accelerates the surface oxygen mobility and lattice oxygen

migration, thus realizing an effective coke elimination [26–30]. In addition to the CO_2 conversion, CH_4 prefers to adsorb onto the Ni surface and undergoes the activation to produce CH_x and H atoms. Thus, a highly dispersed Ni particle with a small size and large exposed area favors a fast CH_4 conversion [31–33]. To ensure a well-distributed and unchanged particle size, metal oxides can be added to interact strongly with Ni sites by forming the solid solution or spinel phase. Moreover, Ni nanoparticle migration could be retarded by the physical steric hindrance provided by the ordered porous or hierarchical metal oxide structures. Based on the above discussion, metal oxides play a crucial role in affecting the physicochemical properties and catalytic performances of Ni-based catalysts in the DRM reaction.

In recent years, reviews on the catalysts for the DRM reaction mainly focus on specific metal or support materials, such as Ni-based catalysts [34], transition metal catalysts [35], Ni/Al_2O_3 catalysts [36], silica-based catalysts [37], Lanthanoid-containing Ni-based catalysts [38], metal carbides [39] and alloy catalysts [40]. Very few works are focused on the applications of metal oxides in Ni-based catalysts relating to the modification impacts on the size, morphology, surface, and interface properties that are based on the catalytic activities and anti-deactivation behaviors in the DRM reaction; therefore, this review summarizes the state-of-art developments of Ni-based catalysts regarding the modification strategies (support confinement, metal–support interaction, oxygen defects, and surface acidity/basicity) of metal oxides (basic oxides, rare earth metal oxides, transition metal oxides, and mixed oxides) on the activity, selectivity, stability, and deactivation resistance in the DRM reaction. Moreover, the reaction and deactivation mechanisms of Ni catalysts in the DRM reaction are illustrated in detail. In addition, the structure–performance relationships are critically discussed in depth. Finally, conclusive remarks and prospects are proposed.

2. Reaction and Deactivation Mechanisms

2.1. Catalytic Reaction Mechanism

In the DRM reaction, an equal amount of CO_2 and CH_4 are transformed into syngas. Due to the strong C-H bonds in CH_4, and the highest valence state of C in CO_2 [41,42], the DRM reaction possesses a highly endothermic nature, as presented below [43]:

$$CH_4 + CO_2 \rightarrow 2CO + 2H_2 \; \Delta H^0_{298} = 247.3 \text{ kJ/mol} \quad (1)$$

As for the reaction mechanisms, mono-functional (on metals only) and bi-functional mechanisms (on metals and supports) are proposed as follows [44]. In the mono-functional pathway (Equations (2)–(10)), the dissociation of CH_4 and CO_2 takes place simultaneously, producing CO, O, H, and CH_x species. Subsequently, CH_x combines with O atoms to form CO and H atoms, whereas two H atoms combine to generate H_2 molecules. In the meantime, hydroxyl groups are produced by the combination of O and H atoms. After hydrogenation, -OH is converted to H_2O as a side product.

$$CH_4 \leftrightarrow CH_{x(Ni)} + (4-x)H_{(Ni)} \quad (2)$$

$$2H_{(Ni)} \leftrightarrow H_{2(gas)} \quad (3)$$

$$CO_{2(gas)} \leftrightarrow CO_{2(Ni)} \quad (4)$$

$$CO_{2(gas)} \leftrightarrow CO_{(Ni)} + O_{(Ni)} \quad (5)$$

$$O_{(Ni)} + CH_{x(Ni)} \leftrightarrow CO_{(Ni)} + xH_{(Ni)} \quad (6)$$

$$CO_{(Ni)} \leftrightarrow CO_{(gas)} \quad (7)$$

$$H_{(Ni)} + O_{(Ni)} \leftrightarrow HO_{(Ni)} \quad (8)$$

$$H_{(Ni)} + HO_{(Ni)} \leftrightarrow H_2O_{(gas)} \quad (9)$$

$$OH_{(Ni)} \leftrightarrow HO_{(support)} \quad (10)$$

In the bi-functional mechanism (Equations (11)–(26)) [45], the activation of CO_2 occurs on the support, whereas that of CH_4 takes place at the Ni surface. In addition, O atoms can be generated from both the -OH decomposition at the Ni sites and the reaction between CO_2 and O^{2-} ions at the support. Subsequently, CO can be produced from both the oxidation of CH_x at the metal surface and the dissociation of $HCO_2{}^-$ from the support derived from the hydrogenation of $CO_3{}^{2-}$ and $HCO_3{}^-$. Instead of the combination of -OH and H atoms in the mono-functional mechanism, two -OH groups react with each other to form the side product H_2O.

CH_4 activation at Ni sites:

$$CH_4 \leftrightarrow CH_{x(Ni)} + (4-x)H_{(Ni)} \quad (11)$$

$$2H_{(Ni)} \leftrightarrow H_{2(gas)} \quad (12)$$

$$OH_{(support)} \leftrightarrow OH_{(Ni)} \quad (13)$$

$$OH_{(Ni)} \leftrightarrow H_{(Ni)} + O_{(Ni)} \quad (14)$$

$$OH_{(Ni)} + H_{(Ni)} \leftrightarrow H_2O_{(gas)} \quad (15)$$

$$O_{(Ni)} + CH_{x(Ni)} \leftrightarrow CO_{(Ni)} + xH_{(Ni)} \quad (16)$$

$$CO_{(Ni)} \leftrightarrow CO_{(gas)} \quad (17)$$

CO_2 activation on support sites:

$$CO_{2(gas)} \leftrightarrow CO_{2(support)} \quad (18)$$

$$CO_{2(support)} + O^{2-}_{(support)} \leftrightarrow CO^{2-}_{3(support)} + O_{(Ni)} \quad (19)$$

$$CO_{2(support)} + OH^{-}_{(support)} \leftrightarrow HCO^{-}_{3(support)} \quad (20)$$

$$H_{(Ni)} \leftrightarrow H_{(support)} \quad (21)$$

$$CO^{2-}_{3(support)} + 2H_{(support)} \leftrightarrow HCO^{-}_{2(support)} + H_2O_{(support)} \quad (22)$$

$$HCO^{-}_{2(support)} \leftrightarrow CO_{(support)} + OH^{-}_{(support)} \quad (23)$$

$$CO_{(support)} \leftrightarrow CO_{(gas)} \quad (24)$$

$$2OH^{-}_{(support)} \leftrightarrow H_2O_{(support)} + O^{2-}_{(support)} \quad (25)$$

$$H_2O_{(support)} \leftrightarrow H_2O_{(gas)} \quad (26)$$

2.2. Deactivation Mechanisms

2.2.1. Coking

In the DRM reaction, coke formation can be caused by CH_4 cracking (Equation (27)) and CO disproportionation (Equation (28)) [46,47], which covers the Ni surface and blocks catalyst pore structures [46]. The impacts of carbon deposits depend on the structure. α-carbon is usually amorphous and mostly formed at the Ni sites with a small size and high dispersion, which is easily gasified during the reaction. In comparison, large Ni particles favor the formation of β-carbon, which is not active as α-carbon, and is possibly transformed into γ-carbon. As the most inert and ordered phase, γ-carbon is in the form of graphite and exerts the most detrimental effect on catalytic activity and stability [48,49].

$$CH_4 \leftrightarrow C + 2H_2 \ \Delta H^0_{298} = 74.9 \text{ kJ/mol} \quad (27)$$

$$2CO \leftrightarrow C + CO_2 \ \Delta H^0_{298} = -172.2 \text{ kJ/mol} \quad (28)$$

The factors determining the coke formation include the particle size, metal–support interaction (MSI), temperature, space-time, and the surface property of catalysts. For example, a large particle size favors the carbon deposition, especially in the form of inert graphitic carbons encapsulating the active sites. As for the MSI, a strong MSI mostly facilitates the coke removal, owing to the interface synergy; however, an excessively strong MSI might lead to the coverage of carbon nanotubes on the active centers. Moreover, a high reaction temperature probably inhibits the carbon formation because the CO disproportionation is greatly prevented; however, the catalyst should be carefully designed to gasify the carbon derived from methane decomposition. Moreover, at a low space-time, a serious deposition of filamentous and encapsulated carbons occurs; at a high space-time, more encapsulated cokes are eliminated, especially with the temperature increase. Finally, a basic and oxygen-deficient catalyst surface enables high CO_2 adsorption and activation with a rapid oxygen migration, which promotes the coke gasification.

2.2.2. Sintering

In high temperature conditions, a large Ni particle is generated following either Ostwald ripening or particle migration mechanism. In Ostwald ripening (atomic migration), which occurs at a relatively higher temperature and has a longer duration, the particle emitted from the metal is captured by another one to form a larger size. In comparison, in particle migration, which prefers lower temperatures, two particles move on the surface of the support and combine to produce a larger particle [50]. Apart from the metal sintering, support sintering is possibly caused by phase transformation or the evaporation/condensation of volatile molecules/atoms [46]. For example, θ-phase Al_2O_3 was transformed into α-phase when the temperature increased from 1000 to 1125 °C, resulting in a reduction in surface area [51]. According to the authors, the reduction of surface area was due to the micropore collapse and dense hcp phase formation. Notably, the transition temperature change initiated by the spinel formation might also be a driving force of the phase transformation.

In addition to the temperature effect, an ordered mesoporous support or a hierarchical structure offers a confinement effect, so as to hinder the random movement of metal particles; however, if the precursor concentration is very high, some metal ions fail to enter the pores and accumulate on the support surface, which easily agglomerate with each other during the subsequent high temperature treatment. Moreover, a fast flow rate of the reducing stream may eliminate the heat generated on the catalyst bed, thus enhancing the metal dispersion.

2.2.3. Poisoning

Due to the existence of impurities (e.g., sulfur species) in the raw feed, metallic Ni is easily converted to sulfides via a reaction with H_2S (Equation (29)) [52]. As a result, the adsorption and activation of CH_4 are inhibited. In addition to the sulfidation mechanism, side reactions or carbon formation might be favored under the coverage of sulfur species.

$$Ni + H_2S \leftrightharpoons Ni - S + H_2 \quad (29)$$

To address the poisoning issues, the increase in reaction temperature is effective to break the Ni-S bond; in other reports, however, a high temperature causes irreversible S layers to form on the active sites, whereas a low temperature favors polysulfide formation, which is easily removed by H_2. As well as the temperature, the introduction of O_2 or steam could alleviate this poisoning effect; however, the oxidation of Ni metals into oxides or sulfates leads to the loss of active sites [50,52]. Moreover, the doping of noble metals may protect the Ni active sites from being poisoned.

3. Impacts of Metal Oxides

To promote the adsorption and activation of reactant molecules and prevent the deactivation of Ni catalysts, metal oxides can be added as either a support or a modifier

so as to confine the Ni particles within the pores or core–shell structures, to anchor the Ni metals via a strong metal-support interaction (MSI), to improve the CO_2 adsorption at the abundant basic sites, and to facilitate the oxygen mobility so as to oxidize the carbon and sulfides. Commonly used metal oxides include basic oxides, rare earth metal oxides, transition metal oxides, and mixed oxides. In the following sections, the impacts of metal oxides on the physicochemical properties and catalytic performances of Ni catalysts in the DRM reaction will be discussed in four categories (support confinement, metal–support interaction, oxygen defects, and surface acidity/basicity).

3.1. Support Confinement

Many oxides with a porous structure exhibit the support confinement effect on the dispersion of metal sites. For example, ordered mesoporous silica materials provide an abundant confined space for inhibiting the metal migration. Benefiting from the ordered channels of SBA-15, negligible metal sintering occurred over a 40 h reaction [53]; however, the other two silica supports (MCM-41 and KIT-6) suffer from the poor structure stability and micropore blocking, resulting in a low activity but high coke formation [54,55]. Similarly, with the silica materials, a metal oxide with ordered porous structures can effectively accommodate the Ni species and prevent the migration of Ni particles, thus improving the anti-sintering property and maintaining the activation of CH_4. Compared with non-porous Al_2O_3, the 2D hexagonal Al_2O_3 support prepared by the "one-pot method" possessed abundant mesopores, offering a confined space for accommodating Ni–Fe alloy particles. The resultant highly dispersed Ni–Fe active sites stabilized the conversion efficiency with negligible metal growth or carbon deposition after 13 h during the DRM reaction at 700 °C (Table 1) [33]. With CeO_2 doped into the framework, the CeO_2–Al_2O_3 mesoporous support structures prevented Ni nanoparticles from migration and agglomeration, keeping the active sites exposed to the reactant molecules. At 700 °C, the CH_4 conversion was as high as 78% over 80 h for the CeO_2-modified catalyst [56]. As well as the 2D morphology, by carefully controlling the pH value in synthesis, the formed mesoporous Al_2O_3 with a cubic phase provided steric hindrance to confine the Ni metals within the support matrix. Owing to the strong resistance against coking and sintering, an excellent conversion of CO_2 and CH_4 were obtained (97% and 99%, respectively), with only 5% coke formation over a 210 h DRM reaction at 700 °C (Table 1) [31]. To simultaneously improve the Ni dispersion and mass diffusion, a hierarchically porous Al_2O_3 structure with bimodal pore distribution (macropore structure and mesoporous channels) confined the Ni nanoparticles, and allowed the fast diffusion of intermediates and products, thus facilitating the CH_4 activation and carbon removal [57].

Table 1. A summary of representative Ni-based catalysts modified with metal oxides for DRM reaction.

Catalyst	Temperature (°C)	CH_4/CO_2	CH_4 Conversion (%)	CO_2 Conversion (%)	H_2/CO	Remark	Ref
$Fe_{5\%}Ni_{5\%}Al_2O_3$	700	1.8:1	50	89	1.1	NiFe alloy particles were confined within the ordered mesoporous Al_2O_3 frameworks.	[33]
Ni/Al_2O_3	850	1:1	99	96	0.89	Cubic and mesoporous Al_2O_3 confined Ni particles and exhibited strong sintering resistance over 210 h.	[31]
$Ni–CeO_2/SiO_2$	700	1:1	77	85	0.95	High Ni dispersion on CeO_2 and abundant Ni–CeO_2 interfaces enhanced the coke resistance.	[58]
Ni/La_2O_3	650	1:1	30	68	0.9	Ni agglomeration was alleviated over 50 h due to the La_2O_3 mesopore confinement.	[59]
$Ni/Y_2O_3–ZrO_2$	700	1:1	67	71	0.85	Ni particle size was reduced over 8 h due to re-dispersion and strong MSI with Y_2O_3 doping.	[60]

Table 1. *Cont.*

Catalyst	Temperature (°C)	CH_4/CO_2	CH_4 Conversion (%)	CO_2 Conversion (%)	H_2/CO	Remark	Ref
$LaNi_{0.34}Co_{0.33}Mn_{0.33}O_3$	800	1:1.05	94	92.5	1.15	MnO enhanced the interaction between the metal and La_2O_3 support.	[61]
Ni/Al_2O_3–$La_2O_3CO_3$	650	1:1	61	65	0.85	$La_2O_2CO_3$ increased the number of Ni active sites by inhibiting the $NiAl_2O_4$ formation.	[32]
Ni/MgO–ZrO_2	800	1:1	68	75	0.89	ZrO_2 tuned the MSI in Ni/MgO and enhanced the reducibility.	[62]
1.5CeO_{2-x}–NSNT	750	1:1	82	88	0.91	Ni silicate nanotubes (NSNTs) reacted with CeO_2 to produce Ce^{3+} and oxygen defects, inhibiting the coke formation.	[28]
$Ce_{0.70}La_{0.20}Ni_{0.10}O_{2-\delta}$	750	1:1	73	84	0.88	Oxygen defects and $La_2O_2CO_3$ contributed to the improved coke resistance.	[29]
$La(Co_{0.1}Ni_{0.9})_{0.5}Fe_{0.5}O_3$	750	1:1	70	80	0.89	Co partial substitution generated oxygen vacancies and enhanced the amount of surface oxygen species.	[30]
$La_{0.4}Ce_{0.6}Ni_{0.5}Fe_{0.5}O_3$	750	1:1	62	72	0.91	Reversible redox reaction and undercoordinated B-site cations increased oxygen defect concentration.	[63]
Co–Ni/Sc-SBA–15	700	1:1	72.5	79	0.91	More basic sites were generated with the Sc doping, reducing the inert carbon amount.	[19]
$SmCoO_3$	800	1:1	93	90	1.1	Co activated CH_4 and $Sm_2O_2CO_3$ removed carbon intermediates.	[24]
Ni/Al_2O_3–MgO	800	1:1	40	52	0.7	MgO enhanced the concentration of medium and strong basic sites, thus alleviating the encapsulated carbon formation.	[25]
Y-doped Ni–Mg–Al double-layered hydroxides	700	1:1	76.2	80.8	0.92	Weak and medium basic sites were introduced by Y_2O_3, promoting reversible CO_2 adsorption and desorption.	[64]

Apart from Al_2O_3, CeO_2 can provide a confinement effect on the Ni particles. Via the one-step colloidal solution combustion method, highly dispersed Ni nanoparticles were formed due to the spatial confinement by CeO_2. During the reaction, Ni migration and agglomeration were greatly inhibited, producing a particle size of less than 5 nm. Owing to the small Ni metal size and abundant Ni–CeO_2 interfaces, only 1.8% carbon deposition was observed over a 20 h DRM reaction at 700 °C (Table 1) [58]. Similarly, mesoporous La_2O_3 was synthesized with SBA-15 as the hard template. As shown in Figure 1, large Ni particles were formed with an average size of 13.7 nm; in comparison, much smaller Ni nanoparticles with a size of 4.6 nm were highly dispersed and confined within the mesopores of La_2O_3. After 50 h of the DRM reaction at 650 °C, serious Ni agglomeration took place in the 5Ni/La_2O_3-n catalyst, such that the particle size was increased to 17.1 nm, whereas for the mesoporous La_2O_3 supported Ni catalyst, a lower degree of metal growth was presented, in that the spent Ni size was 5.5 nm. As well as the abundant active sites for CH_4 activation, a higher dispersion and smaller size of Ni provided more Ni–La_2O_3 interfaces, where CO_2 adsorption, bidentate carbonate formation, and coke removal were facilitated (Table 1) [59]. Different from a mesoporous structure, as a protective layer, ZrO_2 was proven effective in confining the Ni particles. By coating a porous ZrO_2 shell onto Ni, the metal phase agglomeration was significantly prevented, leading to a much smaller size (6 vs. 170 nm) over 20 h during the DRM reaction at 700 °C [21].

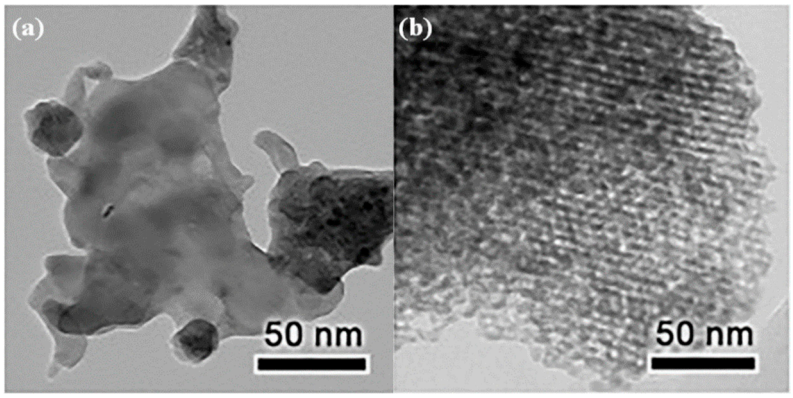

Figure 1. TEM image of a reduced (**a**) 5Ni/La_2O_3-n catalyst (from nitrate) and (**b**) a 5Ni/La_2O_3-m catalyst (with template). Reproduced with permission from [59]. Copyright 2019, Elsevier.

3.2. Metal–Support Interaction

Apart from the physical steric hindrance from the support via confinement effect, the chemical interaction between the Ni and support strengthens the contact at the interface and generates a synergy, thus alleviating the Ni agglomeration and promoting the activation of reactants. For example, unlike other reports where spinel phases are prone to deactivating the catalysts, in Jabbour's study, the $NiAl_2O_4$ spinel phase was formed under air calcination at 700 °C, which enhanced the interaction between Ni and Al_2O_3, producing a small Ni size of only 5 nm. As mentioned earlier, amorphous carbon species prefer to form at small metal sites, which are easily removed during the reaction; therefore, the carbon deposition was as low as 3.8% over the 20 h DRM reaction at 700 °C. Moreover, the CO_2 and CH_4 conversions were both enhanced up to 85.4% and 77.6%, respectively, owing to abundant Ni active sites and large specific surface area [33]. In another work, an interesting finding was presented, stating that Ni metals were partially extracted from the $NiAl_2O_4$ spinel phase, and the resulting Ni active sites were likely anchored by the deficient $Ni_xAl_yO_z$ structure (defective Al_2O_3–NiO solid solution) with multiple Ni^{2+} defects, and thus they favored the strong MSI and coke resistance. Compared with 37% carbon deposition in the controlled Ni/Al_2O_3, the partially reduced $NiAl_2O_4$ exhibited a much lower coke formation (8%) over the 100 h DRM reaction at 700 °C [65]. In addition to the $NiAl_2O_4$ spinel formation, the MSI could be improved when Y_2O_3 was doped in the Ni/ZrO_2. In particular, the reduction temperature (β-peak) shifted to higher temperature regions and the total peak intensity decreased compared with the undoped Ni/ZrO_2 (0.37 vs. 0.62 mmol H_2/g), which indicated that the enhanced MSI derived from the formation of the NiO-ZrO_2 or NiO-Y_2O_3 solid solution. Owing to the strong MSI and Ni re-dispersion, the Ni particle size in the Y_2O_3-promoted Ni/ZrO_2 catalyst decreased from 16 nm to 10 nm, whereas the pristine Ni/ZrO_2 catalyst exhibited a severe metal growth from 12 nm to 24 nm over the 8 h DRM reaction at 700 °C. Moreover, the coke formation of the Y_2O_3-modified sample was only 1.0%, much smaller than that of the unmodified counterpart (3.7%) (Table 1) [60]. As well as Y_2O_3, the MSI was strengthened when the Ni/C catalyst was doped with CeO_2. The average Ni particle size was reduced from 31.1 nm to 27.6 nm and negligible metal growth was presented after the reaction (27.6 nm vs. 27.9 nm) [66]. The enhanced MSI was also observed when CeO_2 was added into Ni/SiO_2, leading to the formation of smaller Ni particles [67]. The promotional effect of MSI was discussed in depth based on the Ni/La_2O_3 catalyst where the CO_2 activation and coke removal were improved [59]. In detail, as shown in Figure 2, the adsorption energy of CO_2 on the pure La_2O_3 support to form monodentate carbonate was similar to the adsorption energy generated when producing bidentate carbonate (−0.94 eV vs. −1.05 eV). In comparison, the CO_2 adsorption energy produced when forming bidentate carbonate at the Ni–La_2O_3 interface was −2.64 eV, which is much lower than that generated when forming monodentate carbonate (−0.12 eV), thus suggesting a greater potential of producing bidentate carbonate upon CO_2 activation at the

interface, rather than the support. Based on the in situ DRIFTS measurement during the adsorption of CH_4, which reacted with the surface carbonates, the intensity of monodentate carbonate was almost unchanged, whereas that of bidentate carbonate showed a gradual decrease, indicating the consumption of carbon intermediates and suppression of cokes at the bidentate carbonate sites. Since bidentate carbonate prefers to form at the Ni–La_2O_3 interface, a strong MSI in Ni/La_2O_3 favored the generation of abundant interfaces, thus potentially reducing the coke formation [59].

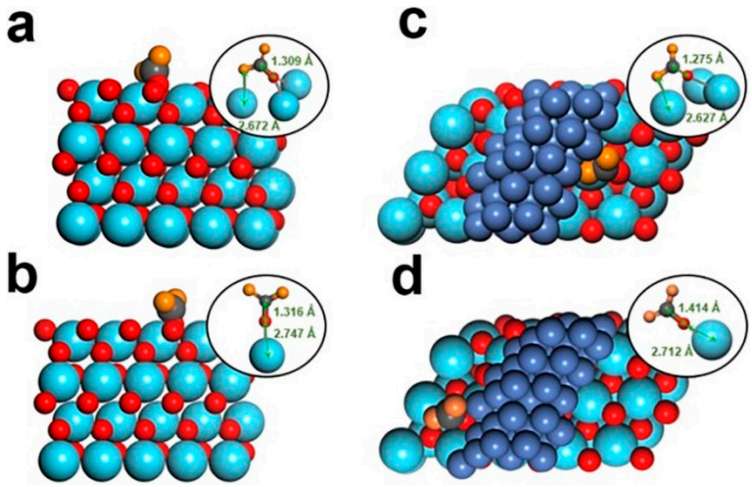

Figure 2. DFT calculations of two modes of CO_2 activation: (**a**,**c**) bidentate carbonate and (**b**,**d**) monodentate carbonate. Colors: Ni—steelblue; C—gray; La—cyan; O—red and orange. Reproduced with permission from [59]. Copyright 2019, Elsevier.

In addition to the rare earth metal oxides, the in situ formed MnO in the Co,Mn-co-doped $LaNi_{0.34}Co_{0.33}Mn_{0.33}O_3$ perovskite structure, strengthened the interaction with both Ni and La_2O_3, thus promoting the coke gasification at the Ni surface. On the contrary, the controlled sample without MnO possessed a relatively weak MSI and suffered from the Ni detachment by the carbon species, subsequently retarding the coke elimination with the nearby O atoms (Figure 3a). In addition, compared with co-doped and unmodified counterparts, $LaNi_{0.34}Co_{0.33}Mn_{0.33}O_3$ exhibited a higher H_2/CO ratio over the 14 h DRM reaction at 800 °C, which could be attributed to the rapid CO_2 conversion and inhibited RWGS reaction at the surface (Figure 3b) (Table 1) [61].

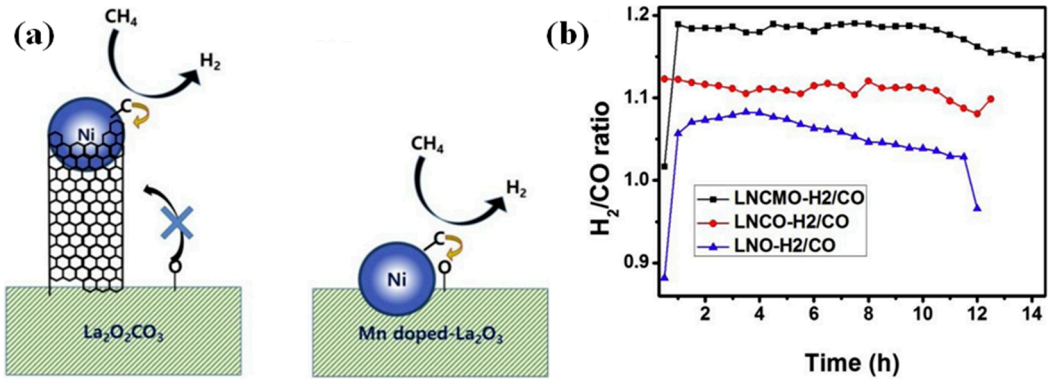

Figure 3. (**a**) Schematic illustration of catalyst deactivation by coking. (**b**) H_2/CO ratio of $LaNi_{0.34}Co_{0.33}Mn_{0.33}O_3$ (LNCMO), $LaNi_{0.5}Co_{0.5}O_3$ (LNCO) and $LaNiO_3$ (LNO). Reproduced with permission from [61]. Copyright 2019, Elsevier.

However, an excessively strong MSI may decrease the active site concentration and intensify the metal agglomeration due to the poor reducibility and too high reduction tem-

peratures [68]. To address this issue, CaO was added to Al_2O_3 to form calcium aluminate, thus weakening the NiO–Al_2O_3 interaction in the spinel phase. Owing to the moderate MSI, abundant Ni active sites were produced for a highly active CH_4 conversion. With the continued increase of CaO loading, however, the interaction between the Ni and support became too weak to anchor the Ni nanoparticles, thus causing Ni agglomeration and surface area reduction; moreover, higher electron density at the Ni surface limited the CH_4 activation, thus deteriorating both the activity and stability [22]. In addition to CaO, rare earth metal oxide La_2O_3 can be utilized as a modifier to adjust the MSI in Ni/Al_2O_3. For example, the monolayer of La_2O_3 strengthened the Al_2O_3–La_2O_3 interaction and inhibited the Ni migration; however, the coverage on the Ni sites reduced the effective exposure of active centers to the reactants. Under CO_2 treatment, $La_2O_2CO_3$ was formed rather than La_2O_3 on the Al_2O_3 surface, which increased the amount of active Ni sites by preventing $NiAl_2O_4$ spinel phase formation. At 650 °C, 61% CH_4, and 65% CO_2 conversions were achieved with only 4% carbon formation (Table 1) [32]. La_2O_3 was also used to tune the MSI of Ni/ZrO_2, that is, a moderate MSI was provided, and the reducibility was enhanced, which produced more active sites for the CO_2 and CH_4 activation, thus resulting in an admirable conversion of CO_2 (>70%) and CH_4 (>60%) at 700 °C; however, CH_4 direct decomposition was promoted by La_2O_3 and carbon filaments and fibers at the Ni surface, which gradually caused the activities to deteriorate over the 67 h DRM reaction at 700 °C [69]. Moreover, La_2O_3, ZrO_2, and CeO_2 were compared in terms of their adjustment of MSI in the Ni/MgO catalyst. In detail, a higher reducibility was achieved with ZrO_2, and the amount of Ni active sites was much higher than that of Ni/CeO_2–MgO (8.12×10^{-7} vs. 3.93×10^{-7} g_{mol}/g_{cat}). As a consequence, more CH_4 molecules were activated with ZrO_2, and more H_2 gas was generated based on the higher H_2/CO ratio of 0.89, compared with that of Ni/CeO_2–MgO (0.78) (Table 1) [62].

3.3. Oxygen Defects

Metal oxides with redox property and oxygen defects accelerate the lattice and surface oxygen migration and enhance the surface oxygen concentration. In both mono-functional and bi-functional mechanisms, the dissociated CH_x intermediates will be effectively gasified by O radicals to produce CO and H adsorbed on the metal sites, thus inhibiting the carbon deposition. Moreover, the high oxygen concentration and fast oxygen mobility benefit the S removal and facilitate the sulfide conversion. For example, the CO_2 adsorption and dissociation were promoted on the ZrO_2 surface with a redox property, thus inhibiting the coke formation [70]. Moreover, H_2-treatment generated more oxygen vacancies in ZrO_2 compared with N_2 and O_2 calcination, which enhanced the CO_2 activation by forming monodentate and bidentate carbonates, thus releasing oxygen species to eliminate the carbon deposits [71]. Similarly, when TiO_2 was doped in Ni/Al_2O_3, the carbon deposition was alleviated owing to the redox ability of TiO_2; however, an excessive amount of TiO_2 might lead to Ni agglomeration, coverage of active sites, and titania structure shrinkage [72]. Apart from the transition metal oxides, CeO_2 presents an impressive oxygen storage capacity and a redox pair of Ce^{3+}/Ce^{4+}, which interacts with Ni via the d–d orbital electron transfer from CeO_2 to Ni. During the reaction, the adsorbed CO_2 will dissociate into CO and O radicals, which oxidizes the carbon species (e.g., CH_x) to produce CO and H atoms (combining to generate H_2); in the meantime, CO_2 reacts with Ce_2O_3 to generate CO and CeO_2. Subsequently, carbon species from CH_4 activation are oxidized by CeO_2 to produce Ce_2O_3 and CO, thus completing the redox cycle of Ce^{3+}/Ce^{4+} and removing the carbon deposits [73]. Additionally, due to the oxygen defects and redox pair of Ce^{3+}/Ce^{4+}, the surface oxygen mobility is promoted, and the content of surface oxygen becomes higher, thus eliminating the carbon effectively [74]. Moreover, owing to the enhanced surface oxygen species in the presence of CeO_2, CO_2 is adsorbed on the surface in the form of bidentate carbonate, which easily combines with carbons so as to maintain the active site as being free from cokes, and to achieve a high conversion efficiency in the DRM reaction [12,75]. When CeO_2 was doped into Ni/Al_2O_3, the $CeAlO_3/CeO_2$ redox

pair was formed, producing abundant oxygen defects and surface oxygen species. Due to the promoted oxygen migration to the interface between Ni and supports, carbon elimination was effectively facilitated, keeping the active sites exposed to the reactants. Moreover, surface carbonates were generated from the reaction between CO_2 and CeO_2, which improved the CH_x conversion and coke resistance. When the Ce loading was increased up to 15 wt%, only 0.29 g/g_{cat} carbon deposition was produced over a 250 h DRM reaction at 800 °C [76]. Similarly, when Ni silicate nanotubes (NSNTs) were doped with CeO_2, both Ce^{3+} and oxygen defects were generated from the interface reaction of CeO_2 and NSNTs. Benefiting from the oxygen migration from the adsorbed CO_2 and unidentate carbonate to the CH_x and C species at the nearby Ni sites, only 6% carbon deposition was produced after 100 h DRM reaction at 750 °C (Table 1) [28]. Despite the abundant oxygen vacancies and promoted oxygen mobility, a careful control of the CeO_2 concentration doped in the catalyst is required because the addition of CeO_2 may reduce the metal–support interaction and produce large metal crystal sites, which lowers the CH_4 activation and causes coke deposition.

To further enhance the oxygen defect concentration, ZrO_2 was integrated with CeO_2 to produce a homogeneous solid solution, $CeZrO_2$, based on the peak at 29.4° in Figure 4a. Given that there were more oxygen defects than CeO_2, as reflected by the higher oxygen storage capacity (165 vs. 125 $\mu mol/g_{cat}$ oxygen uptake), the carbon deposition was alleviated according to the higher intensity ratio of the D-band at 1356 cm^{-1} (amorphous carbon) to G-band at 1580 cm^{-1} (ordered carbon) (Figure 4b). Moreover, the Ni oxidation was also inhibited since the oxygen species were consumed by the redox cycle and the oxygen vacancies of the mixed oxides [77]. Similar to $CeZrO_2$, another mixed oxide $Ce_{0.70}La_{0.20}Ni_{0.10}O_{2-\delta}$ was applied in the DRM reaction, owing to the oxygen defects formed when the lattice expansion and partial dissolution of La^{3+} occurred. Additionally, more oxygen vacancies were produced with the increase in reduction temperatures. Benefiting from the oxygen defect, lattice oxygen migration from CeO_2 was accelerated, oxidizing Ni–C to produce Ce^{3+} species, Ni metals and CO molecules. Moreover, carbon deposits could be converted to CO by reacting with $La_2O_2CO_3$. As a result, zero coke formations were observed over the 50 h DRM reaction at 750 °C (Table 1) [29].

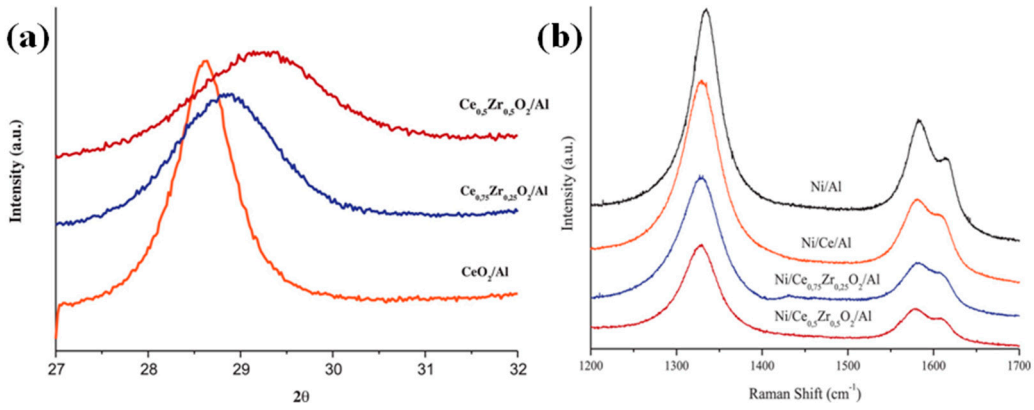

Figure 4. (**a**) XRD patterns of fresh support materials. (**b**) Raman spectra of used catalysts. Reproduced with permission from [77]. Copyright 2014, Elsevier.

In addition to CeO_2, other rare earth metal oxides are characterized with a good oxygen storage capacity and redox potential. For example, the addition of Y_2O_3 enhanced the surface oxygen concentration and accelerated the oxygen transfer to the carbon species, thus effectively eliminating the cokes and retaining the catalytic stability [78]. As well as the intrinsic oxygen defects, more oxygen vacancies could be generated due to the Ni^{2+}/Sm^{3+} ion exchange. As a result, Sm_2O_3-modified Ni catalysts exhibited a low carbon formation and stabilized CH_4 activation [79]. Zhang et al. [80] compared a series of rare earth metal oxides with the promoter of Ni/ZrO_2, based on the impact on the oxygen defects. The

Y-doped catalyst possessed the largest amount of surface oxygen species, followed by Ni/ZrO_2 doped with Sm, La, Ce, and no dopant. Although the activation of CH_4 and CO_2 were facilitated in the presence of oxygen species, the coke deposition and elimination did not follow the same trend. In particular, at a low reaction temperature (e.g., 600 °C), CH_4 activation at the surface oxygen sites dominated the reaction pathway so that the formed carbon species might not be immediately removed, thus producing carbon deposits. On the contrary, when the reaction temperature was high (e.g., 800 °C), CO_2 activation caught up with the CH_4 dissociation, effectively removing the carbon species.

Different from above cases, $LaAlO_3$ perovskite mixed oxides were formed when Ni/Al_2O_3 was doped with La_2O_3. Compared with pristine Ni/Al_2O_3, the $NiO–Al_2O_3$ interaction was weakened due to the oxygen defects of $LaNiO_3$, and more active sites were produced for a better C–H activation, delivering a 37.2% increase of the H_2 yield over the 20 h DRM reaction at 700 °C. Interestingly, both unmodified and modified catalysts exhibited the formation of carbon nanotubes (CNTs); however, unlike most of the reported works, the catalytic activity of $LaNiO_3$ was promoted by CNTs in this instance, since the Ni active sites were located at the tip of CNTs due to the weakened MSI and metal detachment from the support surface, thus being fully exposed to the reactant molecules. In comparison, the Ni metals were anchored on the Al_2O_3 support surface for the Ni/Al_2O_3 catalyst, which resulted in metal growth from the neck (34.9 vs. 16.1 nm after the 10 h reaction) and possible coverage by the carbon clusters (Figure 5a) [81].

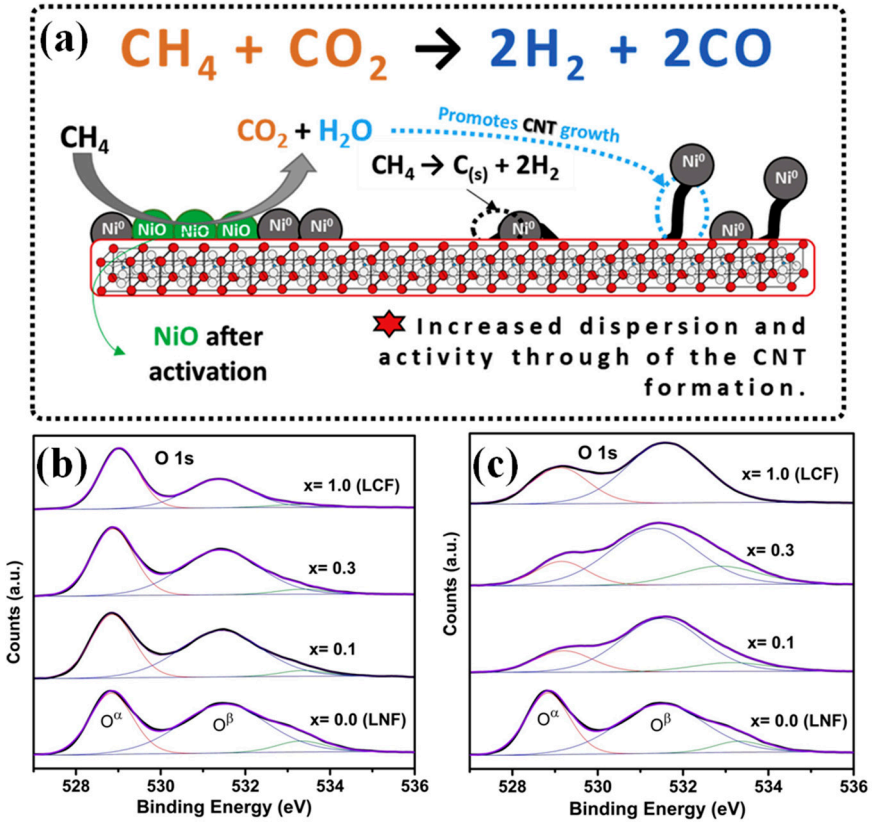

Figure 5. (**a**) Carbon nanotube formation scheme on Ni/Al_2O_3 modified with La_2O_3. Reproduced with permission from [81]. Copyright 2018, Elsevier. (**b**) XPS profiles of O 1 s of the (**b**) fresh and (**c**) spent $La(Co_xNi_{1-x})_{0.5}Fe_{0.5}O_3$ with x = 0.0, 0.1, 0.3, and 1.0. Reproduced with permission from [30]. Copyright 2019, Elsevier.

As for the perovskite structures, B-site modification is proven effective to enhance the oxygen defects. In the Fe-doped $LaNi_{0.8}Fe_{0.2}O_3$ catalyst, Fe_3O_4 was formed during the Fe oxidation by CO_2. Subsequently, La_2O_3 reacted with Fe_3O_4 to form $LaFeO_{3-\delta}$ with

lattice distortion. To compensate for the low valence state of Fe ions, oxygen defects were generated and promoted with the coke elimination [82]. To further modify the perovskite structure of $LaNi_{0.5}Fe_{0.5}O_3$, a series of Co was doped to substitute the B site ions. According to Figure 5b,c, O_β at 531.4 eV referred to the surface oxygen species (e.g., carbonate and hydroxyl groups), whereas O_α at 528.9 eV represented the lattice oxygen. A higher ratio of O_β/O_α indicated a higher percentage of surface oxygen, which could be ascribed to the in situ formed oxygen defects of $LaFeO_3$ perovskite mixed oxides and undercoordinated B-site cations [63,83]. Moreover, the partial substitution of Co ions (0.1 and 0.3) exhibited the largest amount of oxygen defects due to the multiple spin and oxidation states of Co species. Furthermore, the La_2O_3 derived from the reduction of $LaNi_xCo_{1-x}Fe_{0.5}O_3$ reacted with adsorbed CO_2 to form $La_2O_2CO_3$, which also contributed to the oxygen species during the reaction [84]. Owing to the facilitated oxygen mobility and enhanced surface oxygen concentration, $La(Co_{0.1}Ni_{0.9})_{0.5}Fe_{0.5}O_3$ and $La(Co_{0.3}Ni_{0.7})_{0.5}Fe_{0.5}O_3$ exhibited a stable conversion of CH_4 (70%) and CO_2 (80%) over the 30 h DRM reaction at 750 °C (Table 1). More excitingly, the coke formation was as low as 0.8 and 1.5 mg_C/g_{cat} for $La(Co_{0.1}Ni_{0.9})_{0.5}Fe_{0.5}O_3$ and $La(Co_{0.3}Ni_{0.7})_{0.5}Fe_{0.5}O_3$, respectively [30]. Similar to the Co and Fe dopings, when Ni ions were partially replaced by Mn ions, the concentration of monoatomic oxygen defects (O^-) was increased and higher oxygen mobility was achieved. Compared with undoped $LaNiO_3$, the peak of graphitic carbon at 1583 cm^{-1} disappeared in the Raman spectra and the intensity of amorphous carbon at around 1300 cm^{-1} was also considerably lowered [85]. In addition to the transition metals, the doping of Ru produced the perovskite structure $Sr_{0.92}Y_{0.08}Ti_{0.98}Ru_{0.02}O_{3+/-\delta}$. Since the p-band of oxygen shifted to the Fermi level, the formed Ru–O bond was weaker than the Ti–O bond, reducing the formation energy of oxygen defects and increasing the surface oxygen concentration [86].

As well as the B-site substitution, partial replacement of La by Sr generated more oxygen defects and accelerated the surface oxygen mobility due to the lattice distortion, leading to an improved coke resistance; however, an excessive amount of Sr doping weakened the Ni–La_2O_3 MSI, thus intensifying the metal sintering and particle growth [87]. In another study where $La_2Zr_{1.44}Ni_{0.56}O_{7-d}$ was modified with Ca and Sr in the A-site, more oxygen vacancies were generated in the Sr-substituted perovskite catalyst because of the lower ZrO_2 concentration at the surface, which exerted a stronger shielding effect in terms of blocking the oxygen defects. As a result of the abundant Ni active sites and more oxygen vacancies at the surface, trace amounts of soft filamentous carbons (0.024 g/g_{cat}) were produced over the 100 h DRM reaction at 800 °C [88]. Apart from the basic metal oxides, rare earth metal oxide CeO_2 also presented a promotional influence on the catalytic performance as an A-site modifier in the $LaNi_{0.5}Fe_{0.5}O_3$ perovskite. In particular, a reversible redox reaction occurred between $(LaCe)(NiFe)O_3$ and CeO_2, where oxygen defects were produced from the redox pair of Ce^{3+}/Ce^{4+}. Additionally, the reduction of B-site cations into undercoordinated states was activated by the Ce^{3+} ions, further increasing the oxygen defect concentration. Owing to the above merits, CH_4 conversion was enhanced due to the metallic-like Ni, whereas CO_2 activation was promoted at the oxygen vacancies. Moreover, the accelerated lattice oxygen migration favored the immediate gasification of carbon deposits, thus maintaining catalytic stability. As a consequence, the $La_{0.4}Ce_{0.6}Ni_{0.5}Fe_{0.5}O_3$ mixed oxide delivered a quite stable conversion of CH_4 (62%) and CO_2 (72%) over the 25 h DRM reaction at 750 °C (Table 1) [63].

Apart from the perovskite mixed oxides, the spinel phase possesses oxygen defects, especially when Ni is doped. For example, Al_2O_3 dissolution in the $MgAl_2O_4$ spinel phase was charge compensated by the cation and oxygen vacancies at the octahedral and tetrahedral sites. The partial replacement of Mg by Ni introduced more oxygen defects in the formed $(Ni,Mg)Al_2O_4$, which facilitated the CO_2 activation and coke removal during the DRM reaction. When the $(Co_{0.375}Ni_{0.375}Mg_{0.25})Al_2O_4$ structure was developed using co-doping into the $(Ni,Mg)Al_2O_4$, 18% of oxygen ions were removed from the structure under reduction, and a highly oxygen-deficient spinel phase was produced, where the sulfur species at the corners, step edges, and facet edges of metal sites were easily oxidized

by the oxygen that migrated from the lattice and surface. As a consequence, after 12 h of the DRM reaction at 850 °C, the activity only dropped by 4% under 20 ppm H_2S [89]; however, oxygen defects might be only a partial explanation of the origin of sulfur-tolerance. In another study, where 20–30 ppm sulfur was fed in the form of dimethyl sulfoxide (DMSO), only NiCo/CeZr exhibited a quite stable CH4 conversion rather than Ni/CeZr or NiCo/CeLa. Since CeLa also provided abundant oxygen vacancies, the origin of sulfur resistance might not be the oxygen defects or mobility. In this case, Ni–Co synergy could be a dominant factor. Moreover, the gradual decrease of H_2/CO ratio suggested the more rapid deactivation of DRM than the RWGS reaction under a sulfur environment [90].

3.4. Surface Acidity/Basicity

CH_4 prefers to be dissociated at the acidic sites at the surface, easily causing the carbon deposition. To address the issue, a stronger basicity and more basic sites usually enable a better adsorption and activation of CO_2, and the produced O radicals effectively oxidize the CH_x and C species. For instance, carbon deposition could be initiated by the acidic sites at the Al_2O_3 surface. To tune the surface acidity and basicity, La_2O_3 can be added to Al_2O_3 to form a La_2O_3-doped Al_2O_3 surface, thus balancing the CO_2 adsorption/activation, coke elimination, and CH_4 dissociation. As well as the O radicals from the activation of adsorbed CO_2 at the basic sites, the $La_2O_2CO_3$ generated from the reaction between La_2O_3 and CO_2 favored the coke removal, producing La_2O_3 and CO [32,91]. In another study when Ni/SiC-foam was doped with La_2O_3, the surface basicity was greatly enhanced based on the much higher peak intensity in the CO_2-TPD profile, owing to the formation of Ni–La_2O_3 nanocomposites (Figure 6a). During the 50 h DRM reaction at 850 °C, less carbon deposition was observed according to TEM (Figure 6b) and TG results (10.1% mass loss) [92]; however, Ni agglomeration might be intensified in the presence of $La_2O_2CO_3$, which adversely affected the catalytic stability in the DRM reaction. Apart from La_2O_3, Sc_2O_3 as a modifier was proven effective in enhancing the basicity of Ni–Co/SBA-15 catalyst. With the 5% and 10% Sc addition, the overall basicity was increased by 32% and 37%, respectively, especially for the medium basic sites. After the 40 h DRM reaction at 700 °C, the amount of inert carbon species was much less than the unmodified Ni–Co/SBA-15, suggesting the ready transformation of graphitic carbon to amorphous carbon with Sc doping was easily gasified to produce CO (Table 1) [19]. In another study where Ga_2O_3 was integrated with SiO_2, the Ga_2O_3-rich surface adsorbed CO_2 in the form of carbonate and bicarbonate species, which promoted the adsorption and activation of CO_2 compared with the pristine SiO_2, where CO_2 only physically or linearly interacted with the support. During the 10 h DRM reaction at 700 °C, the carbon formation was reduced by 53% [20].

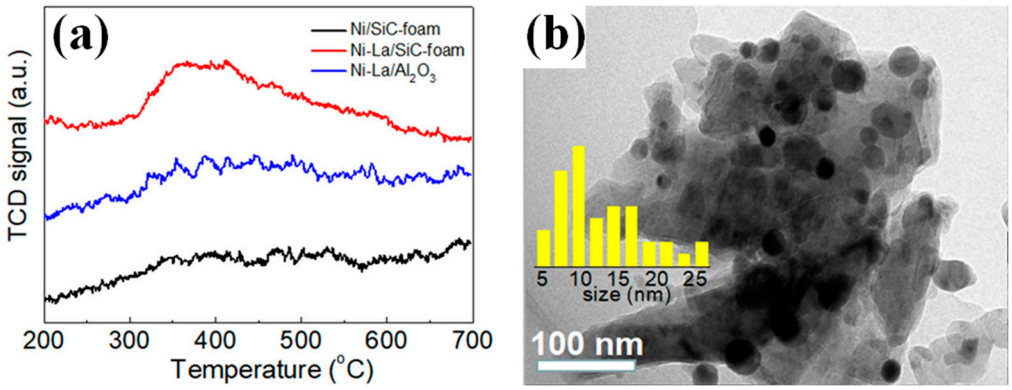

Figure 6. (**a**) CO_2–TPD profiles of spent catalysts. (**b**) TEM images of spent Ni–La_2O_3/SiC-foam. Reproduced with permission from [92]. Copyright 2021, Elsevier.

As well as the enhanced basicity of Al_2O_3 with La_2O_3 addition, the doping of Sr into the A-site deficient $La_{0.8}Cr_{0.85}Ni_{0.15}O_3$ produced $La_{0.6}Sr_{0.2}Cr_{0.85}Ni_{0.15}O_3$, which enhanced

the amount of both weak and strong basic sites. Owing to the improved CO_2 adsorption and activation, CO_2 conversions were increased, and more oxygen radicals were generated, which subsequently gasified the carbon species. In the meantime, CH_4 activation was promoted by the sufficiently small Ni nanoparticles. During the 24 h DRM reaction at 750 °C, both CO_2 and CH_4 conversions reached a high value of 89%; more crucially, zero coke formations were found with this condition [23]. In another study where $SmCoO_3$ perovskite mixed oxides were applied as the catalyst, both medium acid and basic sites were observed based on the CO_2- and NH_3-TPD characterizations, relating to the Sm_2O_3 and Co species, respectively. In particular, CH_4 preferred to be activated at the Co sites where CH_x intermediates and carbon deposits were formed. At the nearby basic Sm sites, $Sm_2O_2CO_3$ was produced from the combination of Sm_2O_3 and CO_2, which converted the carbon intermediates and deposits into CO with a simultaneous Sm_2O_3 regeneration. As a consequence, over 90% of the CH_4 and CO_2 conversions were approached during the 30 h DRM reaction at 800 °C (Table 1) [24].

The strength of basicity also determines the CO_2 adsorption and conversion as well as the carbon elimination. For example, only weak basic sites were present on the unmodified Ni/Al_2O_3 surface; when the MgO was added, the concentration of medium and strong basic sites was increased, which promoted the CO_2 adsorption at hydroxyl groups and activation into the oxygen radicals responsible for the coke removal. As a consequence, the CH_4 conversion was enhanced up to 1780 $L_{CH4}\ g_{Ni}{}^{-1}\ h^{-1}$, thus outperforming the pristine Ni/Al_2O_3 by 26%. Moreover, 70% carbon reduction was realized and most of the eliminated cokes were in the form of detrimental encapsulated carbons (Table 1) [25]. Although a higher basicity and CO_2 adsorption can be obtained with the addition of MgO, the NiO-MgO solid solution may cause the MSI to be too strong, thus retarding the reduction, limiting the active sites, and causing metal sintering due to the high reduction temperature, which lowers the surface area and deteriorates the lifespan of the catalysts. To balance the basicity and MSI, the ratio of MgO and Al_2O_3 was optimized to enable a basic surface where coking was retarded and the RWGS reaction was inhibited, leading to a stable conversion and high H_2 selectivity. In particular, with the Mg/Al ratio increasing from 0.1 to 0.24, the coke formation was reduced by 2/3 due to the enhanced basicity; however, an excessive amount of MgO (Mg/Al = 0.5) adversely affected the performance since the surface area and mesoporous structure were both diminished [93]. Owing to the strong basicity and well-retained mesopores, Ni-DS19 (Mg/Al = 0.24) exhibited a better stability (30 h without reactor plugging) and lower carbon deposition rate than its other two counterparts (Figure 7). In addition to MgO, Y_2O_3 was doped to adjust the basicity of Al_2O_3 by introducing more weak and medium basic sites. Benefiting from the reversible CO_2 adsorption and desorption, coke deposition was significantly reduced, and negligible activity degradation (0.8% for CO_2 and 1.1% for CH_4) was observed during the 10 h DRM reaction at 700 °C [64]. In another study, the total basic site concentration of Ni/ZrO_2 was increased from 73 to 100 μmol CO_2/g with the doping of Y_2O_3. More importantly, the percentage of weak and medium basic sites was enhanced from 79.9% to 87%, favoring the formation of active surface carbonate species and subsequent oxidation of cokes [60]. Similarly, weak and medium basic sites were introduced to Ni/Mg-Al double-layered hydroxides with the addition of Y_2O_3. Owing to the promoted CO_2 activation, about a 10% increase of CH_4 conversion was obtained in the 1.5 wt% Y_2O_3-promoted catalyst at 700 °C. Moreover, the conversion of CH_4 dropped by 4% over 10 h in the unmodified catalyst, whereas that of the Y_2O_3-doped catalyst was only 1% [64].

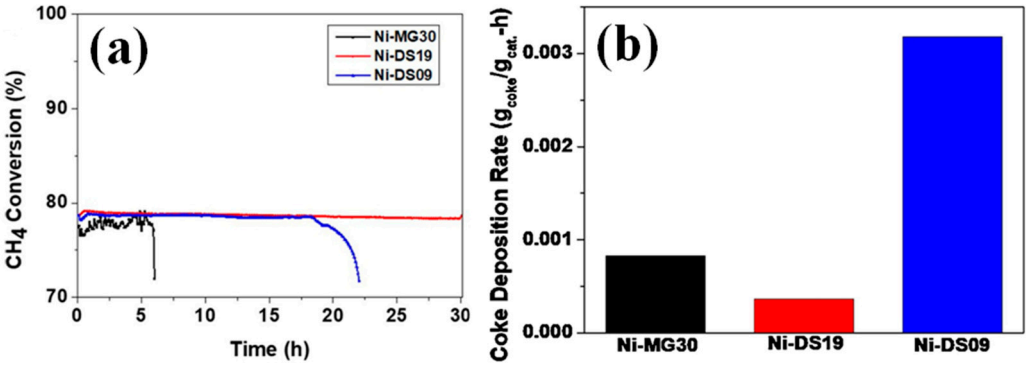

Figure 7. (**a**) CH_4 conversions and (**b**) carbon deposition rates of Ni-MG30 (Mg/Al = 0.5), Ni-DS19 (Mg/Al = 0.24), and Ni-DS09 (Mg/Al = 0.1). Reproduced with permission from [93]. Copyright 2020, Elsevier.

4. Conclusive Remarks and Prospect

In this review, four modification strategies to improve the catalytic performances of Ni-based catalysts in the DRM reaction are critically discussed based on four types of metal oxides (basic oxides, rare earth metal oxides, transition metal oxides, and mixed oxides). In the support confinement section, order porous support structures and hierarchical core-shell designs are proven effective in controlling Ni size and dispersion in high temperature conditions, thus maintaining the number of active sites for the activation of reactant molecules. As for the metal-support interaction, solid solution or spinel phase formation contributes to the highly distributed Ni crystals which strongly interact with the matrix via chemical bonding, thus inhibiting the coke formation; however, when the MSI is too strong, it may lower the reducibility and initiate the metal sintering. For the oxygen defects, redox property and lattice distortion are the main origins of oxygen vacancies, which facilitate the lattice and surface oxygen migration and enhance the surface oxygen concentration, resulting in an efficient elimination of carbon deposits and metal sulfides. As to the surface basicity, medium basicity might be favored in most cases since CO_2 only physically adsorbs onto the weak basic sites, whereas activation is reluctant at basic sites that are too strong. The reversible adsorption of CO_2 benefits the dissociation into CO and O radicals and the formation of active carbonates, which further converts the carbon intermediates or deposits into gaseous products. Despite the achievements in related fields, several issues and possible solutions are proposed as below.

First, there is a debate regarding the impacts of $NiAl_2O_4$. In particular, the Ni metal particles extracted from the spinel phase may interact strongly with the matrix which prevents the metal sintering; on the other hand, the low reducibility might be a concern for effective activation during the reaction; therefore, efforts should be put into the clarification of the effects of spinel phase on the concentration and agglomeration of active sites.

Second, the influences of in situ formed carbon nanotubes (CNTs) are still unclear. In certain scenarios where the Ni detachment occurs due to the weak MSI, the activity may not be adversely affected since the Ni sites located at the tip still activate the CH_4; however, in other cases where metals are strongly anchored at the support surface, CNTs might cover the Ni phase and intensify the metal growth from the neck, which would be encapsulated by carbon clusters. An in-depth study is recommended to monitor the reaction progress and elucidate the critical impacts of CNTs in different conditions.

Third, oxygen defects have been reported as being effective in improving sulfur resistance when metal oxides with multiple valence states and redox properties are doped in the catalysts; however, owing to the fact that some metal oxides with oxygen vacancies still suffer the deactivation caused by the S poisons, other determining factors need to be explored.

Fourth, CH_4 activation at the acidic sites and CO_2 dissociation at the basic sites need to be well balanced with the help of multi-functional metal oxides, which possess both

acidic and basic groups. To address the issue, the co-existence of these two types of sites in mixed oxides or co-supports with Ni doping are promising solutions to simultaneously activate the CH_4 and remove the carbon intermediates.

Author Contributions: Conceptualization, data curation, investigation, writing—original draft, X.G., W.L., Z.G., H.G.; writing—review and editing; X.G.; project administration, supervision, validation, S.K.; funding acquisition, resources, S.K. All authors have read and agreed to the published version of the manuscript.

Funding: This research was funded by NUS Green Energy Program (WBS: A-0005323-05-00), FRC MOE T1 (WBS: A-0009184-00-00), A*STAR LCERFI Project (Award ID: U2102d2011: WBS No. A-8000278-00-00), Guangzhou Basic and Applied Basic Research Project in China: 202102020134; Youth Innovation Talents Project of Guangdong Universities (natural science): 2019KQNCX098.

Data Availability Statement: Not applicable.

Conflicts of Interest: The authors declare no conflict of interest.

References

1. Ashok, J.; Ang, M.; Kawi, S. Enhanced activity of CO_2 methanation over Ni/CeO_2-ZrO_2 catalysts: Influence of preparation methods. *Catal. Today* **2016**, *281*, 304–311. [CrossRef]
2. Ashok, J.; Pati, S.; Hongmanorom, P.; Tianxi, Z.; Junmei, C.; Kawi, S. A review of recent catalyst advances in CO_2 methanation processes. *Catal. Today* **2020**, *356*, 471–489. [CrossRef]
3. Hongmanorom, P.; Ashok, J.; Zhang, G.; Bian, Z.; Wai, M.H.; Zeng, Y.; Xi, S.; Borgna, A.; Kawi, S. Enhanced performance and selectivity of CO_2 methanation over phyllosilicate structure derived Ni-Mg/SBA-15 catalysts. *Appl. Catal. B Environ.* **2020**, *282*, 119564. [CrossRef]
4. Oh, T.H. Carbon capture and storage potential in coal-fired plant in Malaysia—A review. *Renew. Sustain. Energy Rev.* **2010**, *14*, 2697–2709. [CrossRef]
5. Alves, H.J.; Junior, C.B.; Niklevicz, R.R.; Frigo, E.P.; Frigo, M.; Coimbra-Araújo, C.H. Overview of hydrogen production technologies from biogas and the applications in fuel cells. *Int. J. Hydrogen Energy* **2013**, *38*, 5215–5225. [CrossRef]
6. Gao, X.; Lin, X.; Xie, X.; Li, J.; Wu, X.; Li, Y.; Kawi, S. Modification strategies of heterogeneous catalysts for water–gas shift reactions. *React. Chem. Eng.* **2022**, *7*, 551–565. [CrossRef]
7. Faramawy, S.; Zaki, T.; Sakr, A.A.E. Natural gas origin, composition, and processing: A review. *J. Nat. Gas Sci. Eng.* **2016**, *34*, 34–54. [CrossRef]
8. Wang, W.; Wang, W.; Chen, S. The effects of hydrogen dilution, carbon monoxide poisoning for a Pt–Ru anode in a proton exchange membrane fuel cell. *Int. J. Hydrogen Energy* **2016**, *41*, 20680–20692. [CrossRef]
9. Charisiou, N.D.; Douvartzides, S.L.; Siakavelas, G.I.; Tzounis, L.; Sebastian, V.; Stolojan, V.; Hinder, S.J.; Baker, M.A.; Polychronopoulou, K.; Goula, M.A. The relationship between reaction temperature and carbon deposition on nickel catalysts based on Al_2O_3, ZrO_2 or SiO_2 supports during the biogas dry reforming reaction. *Catalysts* **2019**, *9*, 676. [CrossRef]
10. Charisiou, N.; Tzounis, L.; Sebastian, V.; Hinder, S.; Baker, M.; Polychronopoulou, K.; Goula, M. Investigating the correlation between deactivation and the carbon deposited on the surface of Ni/Al_2O_3 and Ni/La_2O_3-Al_2O_3 catalysts during the biogas reforming reaction. *Appl. Surf. Sci.* **2019**, *474*, 42–56. [CrossRef]
11. Gao, X.; Lin, Z.; Li, T.; Huang, L.; Zhang, J.; Askari, S.; Dewangan, N.; Jangam, A.; Kawi, S. Recent Developments in Dielectric Barrier Discharge Plasma-Assisted Catalytic Dry Reforming of Methane over Ni-Based Catalysts. *Catalysts* **2021**, *11*, 455. [CrossRef]
12. Gao, X.; Ashok, J.; Kawi, S. A review on roles of pretreatment atmospheres for the preparation of efficient Ni-based catalysts. *Catal. Today* **2021**, *397–399*, 581–591. [CrossRef]
13. Damyanova, S.; Shterevaa, I.; Pawelecb, B.; Mihaylovc, L.; Fierro, J.L.G. Characterization of none and yttrium-modified Ni-based catalysts for dry reforming of methane. *Appl. Catal. B Environ.* **2000**, *278*, 119335. [CrossRef]
14. Dewangan, N.; Hui, W.M.; Jayaprakash, S.; Bawah, A.R.; Poerjoto, A.J.; Jie, T.; Ashok, J.; Hidajat, K.; Kawi, S. Recent progress on layered double hydroxide (LDH) derived metal-based catalysts for CO_2 conversion to valuable chemicals. *Catal. Today* **2020**, *356*, 490–513. [CrossRef]
15. Das, S.; Ashok, J.; Bian, Z.; Dewangan, N.; Wai, M.; Du, Y.; Borgna, A.; Hidajat, K.; Kawi, S. Silica–Ceria sandwiched Ni core–shell catalyst for low temperature dry reforming of biogas: Coke resistance and mechanistic insights. *Appl. Catal. B Environ.* **2018**, *230*, 220–236. [CrossRef]
16. Sutthiumporn, K.; Kawi, S. Promotional effect of alkaline earth over Ni–La_2O_3 catalyst for CO_2 reforming of CH_4: Role of surface oxygen species on H_2 production and carbon suppression. *Int. J. Hydrogen Energy* **2011**, *36*, 14435–14446. [CrossRef]
17. Gao, X.; Li, J.; Zheng, M.; Cai, S.; Zhang, J.; Askari, S.; Dewangan, N.; Ashok, J.; Kawi, S. Recent progress in anti-coking Ni catalysts for thermo-catalytic conversion of greenhouse gases. *Process Saf. Environ. Prot.* **2021**, *156*, 598–616. [CrossRef]

18. Bian, Z.; Wang, Z.; Jiang, B.; Hongmanorom, P.; Zhong, W.; Kawi, S. A review on perovskite catalysts for reforming of me-thane to hydrogen production. *Renew. Sustain. Energ. Rev.* **2020**, *134*, 110291. [CrossRef]
19. Al-Fatesh, A.S.; Arafat, Y.; Ibrahim, A.A.; Atia, H.; Fakeeha, A.H.; Armbruster, U.; Abasaeed, A.E.; Frusteri, F. Evaluation of Co-Ni/Sc-SBA–15 as a novel coke resistant catalyst for syngas production via CO_2 reforming of methane. *Appl. Catal. A Gen.* **2018**, *567*, 102–111. [CrossRef]
20. Pan, X.Y.; Kuai, P.; Liu, Y.; Ge, Q.; Liu, C.J. Promotion effects of Ga_2O_3 on CO_2 adsorption and conversion over a SiO_2-supported Nicatalyst. *Energy Environ. Sci.* **2010**, *3*, 1322–1325. [CrossRef]
21. Dou, J.; Zhang, R.; Hao, X.; Bao, Z.; Wu, T.; Wang, B.; Yu, F. Sandwiched SiO_2@Ni@ZrO_2 as a coke resistant nanocatalyst for dry reforming of methane. *Appl. Catal. B Environ.* **2019**, *254*, 612–623. [CrossRef]
22. Dias, J.; Assaf, J. Influence of calcium content in Ni/CaO/γ-Al_2O_3 catalysts for CO_2-reforming of methane. *Catal. Today* **2003**, *85*, 59–68. [CrossRef]
23. Wei, T.; Jia, L.; Luo, J.-L.; Chi, B.; Pu, J.; Li, J. CO_2 dry reforming of CH_4 with Sr and Ni co-doped $LaCrO_3$ perovskite catalysts. *Appl. Surf. Sci.* **2019**, *506*, 144699. [CrossRef]
24. Osazuwa, O.U.; Cheng, C.K. Catalytic conversion of methane and carbon dioxide (greenhouse gases) into syngas over sa-marium–cobalt-trioxides perovskite catalyst. *J. Clean. Prod.* **2017**, *148*, 202–211. [CrossRef]
25. Jin, B.; Li, S.; Liang, X. Enhanced activity and stability of MgO-promoted Ni/Al_2O_3 catalyst for dry reforming of methane: Role of MgO. *Fuel* **2020**, *284*, 119082. [CrossRef]
26. Oemar, U.; Hidajat, K.; Kawi, S. Pd–Ni catalyst over spherical nanostructured Y_2O_3 support for oxy-CO_2 reforming of methane: Role of surface oxygen mobility. *Int. J. Hydrogen Energy* **2015**, *40*, 12227–12238. [CrossRef]
27. Li, Z.; Kathiraser, Y.; Kawi, S. Facile Synthesis of Multi-Ni-Core@Ni Phyllosilicate@CeO_2 Shell Hollow Spheres with High Oxygen Vacancy Concentration for Dry Reforming of CH_4. *ChemCatChem* **2018**, *10*, 2994–3001. [CrossRef]
28. Guo, D.; Lu, Y.; Ruan, Y.Z.; Zhao, Y.F.; Zhao, Y.J.; Wang, S.P.; Ma, X.B. Effects of extrinsic defects originating from the inter-facial reaction of CeO_2–x–nickel silicate on catalytic performance in methane dry reforming. *Appl. Catal. B Environ.* **2020**, *277*, 119278. [CrossRef]
29. Pino, L.; Italiano, C.; Vita, A.; Laganà, M.; Recupero, V. $Ce_{0.70}La_{0.20}Ni_{0.10}O_{2-\delta}$ catalyst for methane dry reforming: Influence of reduction temperature on the catalytic activity and stability. *Appl. Catal. B Environ.* **2017**, *218*, 779–792. [CrossRef]
30. Wang, H.Q.; Dong, X.L.; Zhao, T.T.; Yu, H.R.; Li, M. Dry reforming of methane over bimetallic Ni–Co catalyst prepared from $La(Co_xNi_{1-x})_{0.5}Fe_{0.5}O_3$ perovskite precursor: Catalytic activity and coking resistance. *Appl. Catal. B Environ.* **2019**, *245*, 302–313. [CrossRef]
31. Gholizadeh, F.; Izadbakhsh, A.; Huang, J.; Zi-Feng, Y. Catalytic performance of cubic ordered mesoporous alumina supported nickel catalysts in dry reforming of methane. *Microporous Mesoporous Mater.* **2020**, *310*, 110616. [CrossRef]
32. Li, K.; Pei, C.; Li, X.; Chen, S.; Zhang, X.; Liu, R.; Gong, J. Dry reforming of methane over $La_2O_2CO_3$-modified Ni/Al_2O_3 cata-lysts with moderate metal support interaction. *Appl. Catal. B Environ.* **2020**, *264*, 118448. [CrossRef]
33. Jabbour, K.; Saad, A.; Inaty, L.; Davidson, A.; Massiani, P.; Hassan, N.E. Ordered mesoporous Fe–Al_2O_3 based-catalysts synthesized via a direct "one-pot" method for the dry reforming of a model biogas mixture. *Int. J. Hydrogen Energy* **2019**, *144*, 14889–14907. [CrossRef]
34. Qin, Z.; Chen, J.; Xie, X.; Luo, X.; Su, T.; Ji, H. CO_2 reforming of CH_4 to syngas over nickel-based catalysts. *Environ. Chem. Lett.* **2020**, *18*, 997–1017. [CrossRef]
35. Guharoy, U.; Reina, T.R.; Liu, J.; Sun, Q.; Gu, S.; Cai, Q. A theoretical overview on the prevention of coking in dry reforming of methane using non-precious transition metal catalysts. *J. CO2 Util.* **2021**, *53*, 101728. [CrossRef]
36. Gao, X.; Ge, Z.; Zhu, G.; Wang, Z.; Ashok, J.; Kawi, S. Anti-Coking and Anti-Sintering Ni/Al_2O_3 Catalysts in the Dry Re-forming of Methane: Recent Progress and Prospects. *Catalysts* **2021**, *11*, 1003. [CrossRef]
37. Taherian, Z.; Khataee, A.; Han, N.; Orooji, Y. Hydrogen production through methane reforming processes using promoted-Ni/mesoporous silica: A review. *J. Ind. Eng. Chem.* **2022**, *107*, 20–30. [CrossRef]
38. Salaev, M.A.; Liotta, L.F.; Vodyankina, O.V. Lanthanoid-containing Ni-based catalysts for dry reforming of methane: A review. *Int. J. Hydrogen Energy* **2022**, *47*, 4489–4535. [CrossRef]
39. Czaplicka, N.; Rogala, A.; Wysocka, I. Metal (Mo, W, Ti) Carbide Catalysts: Synthesis and Application as Alternative Catalysts for Dry Reforming of Hydrocarbons—A Review. *Int. J. Mol. Sci.* **2021**, *22*, 12337. [CrossRef] [PubMed]
40. Torimoto, M.; Sekine, Y. Effects of alloying for steam or dry reforming of methane: A review of recent studies. *Catal. Sci. Technol.* **2022**, *12*, 3387–3411. [CrossRef]
41. Wang, Y.; Yao, L.; Wang, S.; Mao, D.; Hu, C. Low-temperature catalytic CO_2 dry reforming of methane on Ni-based catalysts: A review. *Fuel Process. Technol.* **2018**, *169*, 199–206. [CrossRef]
42. Zhang, G.; Liu, J.; Xu, Y.; Sun, Y. A review of CH_4CO_2 reforming to synthesis gas over Ni-based catalysts in recent years (2010–2017). *Int. J. Hydrogen Energy* **2018**, *43*, 15030–15054. [CrossRef]
43. Aghaali, M.H.; Firoozi, S. Enhancing the catalytic performance of Co substituted $NiAl_2O_4$ spinel by ultrasonic spray pyrolysis method for steam and dry reforming of methane. *Int. J. Hydrogen Energy* **2020**, *46*, 357–373. [CrossRef]
44. Ranjekar, A.M.; Yadav, G.D. Dry reforming of methane for syngas production: A review and assessment of catalyst development and efficacy. *J. Indian Chem. Soc.* **2021**, *98*, 100002. [CrossRef]

45. Ferreira-Aparicio, P.; Rodríguez-Ramos, I.; Anderson, J.A.; Guerrero-Ruiz, A. Mechanistic aspects of the dry reforming of methane over ruthenium catalysts. *Appl. Catal. A Gen.* **2000**, *202*, 183–196. [CrossRef]
46. Minh, D.P.; Pham, X.H.; Siang, T.; Vo, D.V.N. Review on the catalytic tri-reforming of methane—Part I: Impact of operating conditions, catalyst deactivation and regeneration. *Appl. Catal. A Gen.* **2021**, *621*, 118202. [CrossRef]
47. Guo, J.; Lou, H.; Zhao, H.; Chai, D.; Zheng, X. Dry reforming of methane over nickel catalysts supported on magnesium aluminate spinels. *Appl. Catal. A Gen.* **2004**, *273*, 75–82. [CrossRef]
48. Wang, R.; Liu, X.; Ge, Q.; Li, W.; Xu, H. Studies of Carbon Deposition over Rh–CeO_2/Al_2O_3 during CH_4/CO_2 Reforming. *Stud. Surf. Sci. Catal.* **2007**, *167*, 379–384.
49. Siang, T.J.; Pham, T.L.; Van Cuong, N.; Phuong, P.T.; Phuc, N.H.H.; Truong, Q.D.; Vo, D.-V.N. Combined steam and CO_2 reforming of methane for syngas production over carbon-resistant boron-promoted Ni/SBA-15 catalysts. *Microporous Mesoporous Mater.* **2018**, *262*, 122–132. [CrossRef]
50. Gao, X.; Wang, Z.; Ashok, J.; Kawi, S. A comprehensive review of anti-coking, anti-poisoning and anti-sintering catalysts for biomass tar reforming reaction. *Chem. Eng. Sci. X* **2020**, *7*, 100065. [CrossRef]
51. Argyle, M.D.; Bartholomew, C.H. Heterogeneous Catalyst Deactivation and Regeneration: A Review. *Catalysts* **2015**, *5*, 145–269. [CrossRef]
52. Chen, X.; Jiang, J.; Yan, F.; Li, K.; Tian, S.; Gao, Y.; Zhou, H. Dry Reforming of Model Biogas on a Ni/SiO_2 Catalyst: Overall Performance and Mechanisms of Sulfur Poisoning and Regeneration. *ACS Sustain. Chem. Eng.* **2017**, *5*, 10248–10257. [CrossRef]
53. Kang, D.; Lim, H.S.; Lee, J.W. Enhanced catalytic activity of methane dry reforming by the confinement of Ni nanoparticles into mesoporous silica. *Int. J. Hydrogen Energy* **2017**, *42*, 11270–11282. [CrossRef]
54. Qian, L.; Huang, K.; Wang, H.; Kung, M.C.; Kung, H.H.; Li, J.; Chen, G.; Du, Q. Evaluation of the catalytic surface of Ni impregnated meso-microporous silica KIT-6 in CH_4 dry reforming by inverse gas chromatography. *Microporous Mesoporous Mater.* **2016**, *243*, 301–310. [CrossRef]
55. Liu, D.; Quek, X.; Cheo, W.N.E.; Lau, R.; Borgna, A.; Yang, Y. MCM-41 supported nickel-based bimetallic catalysts with superior stability during carbon dioxide reforming of methane: Effect of strong metal–support interaction. *J. Catal.* **2009**, *266*, 380–390. [CrossRef]
56. Wang, N.; Xu, Z.; Deng, J.; Shen, K.; Yu, X.; Qian, W.; Chu, W.; Wei, F. One-pot Synthesis of Ordered Mesoporous NiCeAl Oxide Catalysts and a Study of Their Performance in Methane Dry Reforming. *ChemCatChem* **2014**, *6*, 1470–1480. [CrossRef]
57. Ma, Q.; Han, Y.; Wei, Q.; Makpal, S.; Gao, X.; Zhang, J.; Zhao, T. Stabilizing Ni on bimodal mesoporous-macroporous alumina with enhanced coke tolerance in dry reforming of methane to syngas. *J. CO2 Util.* **2020**, *35*, 288–297. [CrossRef]
58. Zhang, C.; Zhang, R.; Liu, H.; Wei, Q.; Gong, D.; Mo, L.; Tao, H.; Cui, S.; Wang, L. One-Step Synthesis of Highly Dispersed and Stable Ni Nanoparticles Confined by CeO_2 on SiO_2 for Dry Reforming of Methane. *Energies* **2020**, *13*, 5956. [CrossRef]
59. Li, K.; Chang, X.; Pei, C.; Li, X.; Chen, S.; Zhang, X.; Assabumrungrat, S.; Zhao, Z.-J.; Zeng, L.; Gong, J. Ordered mesoporous Ni/La_2O_3 catalysts with interfacial synergism towards CO_2 activation in dry reforming of methane. *Appl. Catal. B Environ.* **2019**, *259*, 118092. [CrossRef]
60. Wang, Y.; Li, L.; Wang, Y.; Da Costa, P.; Hu, C. Highly Carbon-Resistant Y Doped NiO–ZrOm Catalysts for Dry Reforming of Methane. *Catalysts* **2019**, *9*, 1055. [CrossRef]
61. Kim, W.Y.; Jang, J.S.; Ra, E.C.; Kim, K.Y.; Kim, E.H.; Lee, J.S. Reduced perovskite $LaNiO_3$ catalysts modified with Co and Mn for low coke formation in dry reforming of methane. *Appl. Catal. A Gen.* **2019**, *575*, 198–203. [CrossRef]
62. Kim, B.J.; Jeon, K.W.; Na, H.S.; Lee, Y.L.; Ahn, S.Y.; Kim, K.J.; Jang, W.J.; Shim, J.O.; Roh, H.S. Reducible oxide (CeO_2, ZrO_2, and CeO_2–ZrO_2) promoted Ni–MgO catalysts for carbon dioxide reforming of methane reaction. *Korean J. Chem. Eng.* **2020**, *37*, 1130–1136. [CrossRef]
63. Wang, M.; Zhao, T.; Dong, X.; Li, M.; Wang, H. Effects of Ce substitution at the A-site of $LaNi_{0.5}Fe_{0.5}O_3$ perovskite on the enhanced catalytic activity for dry reforming of methane. *Appl. Catal. B* **2018**, *224*, 214–221. [CrossRef]
64. Wirk, K.; Gálvez, M.E.; Motak, M.; Grzybek, T.; Rønning, M.; Da Costa, P. Yttrium promoted Ni-based double-layered hydroxides for dry methane Reforming. *J. CO2 Util.* **2018**, *27*, 247–258.
65. Zhou, L.; Li, L.; Wei, N.; Li, J.; Basset, J.-M. Effect of $NiAl_2O_4$ Formation on Ni/Al_2O_3 Stability during Dry Reforming of Me-thane. *ChemCatChem* **2015**, *7*, 2508–2516. [CrossRef]
66. Wang, H.; Zhao, B.; Qin, L.; Wang, Y.; Yu, F.; Han, J. Non-thermal plasma-enhanced dry reforming of methane and CO_2 over Ce-promoted Ni/C catalysts. *Mol. Catal.* **2020**, *485*, 110821. [CrossRef]
67. Guo, Y.; Tian, L.; Yan, W.; Qi, R.; Tu, W.; Wang, Z. CeO_2-Promoted Ni/SiO_2 Catalysts for Carbon Dioxide Reforming of Me-thane: The Effect of Introduction Methodologies. *Catal. Lett.* **2021**, *151*, 2144–2152. [CrossRef]
68. Mette, K.; Kühl, S.; Tarasov, A.; Willinger, M.G.; Kröhnert, J.; Wrabetz, S.; Trunschke, A.; Scherzer, M.; Girgsdies, F.; Düdder, H.; et al. High-Temperature Stable Ni Nanoparticles for the Dry Reforming of Methane. *ACS Catal.* **2016**, *6*, 7238–7248. [CrossRef]
69. Lanre, M.S.; Al-Fatesh, A.S.; Fakeeha, A.H.; Kasim, S.O.; Ibrahim, A.A.; Al-Awadi, A.S.; Al-Zahrani, A.A.; Abasaeed, A.E. Catalytic Performance of Lanthanum Promoted Ni/ZrO_2 for Carbon Dioxide Reforming of Methane. *Processes* **2020**, *8*, 1502. [CrossRef]
70. Ibrahim, A.A.; Al-Fatesh, A.S.; Khan, W.U.; Kasim, S.O.; Abasaeed, A.E.; Fakeeha, A.H.; Bonura, G.; Frusteri, F. Enhanced coke suppression by using phosphate-zirconia supported nickel catalysts under dry methane reforming conditions. *Int. J. Hydrogen Energy* **2019**, *44*, 27784–27794. [CrossRef]

71. Zhang, M.; Zhang, J.; Wu, Y.; Pan, J.; Zhang, Q.; Tan, Y.; Han, Y. Insight into the effects of the oxygen species over Ni/ZrO_2 catalyst surface on methane reforming with carbon dioxide. *Appl. Catal. B Environ.* **2018**, *244*, 427–437. [CrossRef]
72. Shah, M.; Bordoloi, A.; Nayak, A.K.; Mondal, P. Effect of Ti/Al ratio on the performance of $Ni/TiO_2–Al_2O_3$ catalyst for methane reforming with CO_2. *Fuel Process. Technol.* **2019**, *192*, 21–35. [CrossRef]
73. Xu, G.; Shi, K.; Gao, Y.; Xu, H.; Wei, Y. Studies of reforming natural gas with carbon dioxide to produce synthesis gas: X. The role of CeO_2 and MgO promoters. *J. Mol. Catal. A Chem.* **1999**, *147*, 47–54. [CrossRef]
74. Jin, B.T.; Shang, Z.Y.; Li, S.G.; Jiang, Y.B.; Gu, X.H.; Liang, X.H. Reforming of methane with carbon dioxide over cerium oxide promoted nickel nanoparticles deposited on 4-channel hollow fibers by atomic layer deposition. *Catal. Sci. Technol.* **2020**, *10*, 3212–3222. [CrossRef]
75. Jawad, A.; Rezaei, F.; Rownaghi, A.A. Highly Efficient $Pt/Mo–Fe/Ni$-Based $Al_2O_3–CeO_2$ Catalysts for Dry Reforming of Me-thane. *Catal. Today* **2019**, *350*, 80–90. [CrossRef]
76. Chen, W.; Zhao, G.; Xue, Q.; Chen, L.; Lu, Y. High carbon-resistance $Ni/CeAlO_3–Al_2O_3$ catalyst for CH_4/CO_2 reforming. *Appl. Catal. B Environ.* **2013**, *136–137*, 260–268. [CrossRef]
77. Faria, E.C.; Neto, R.C.R.; Colman, R.C.; Noronha, F.B. Hydrogen production through CO_2 reforming of methane over $Ni/CeZrO_2/Al_2O_3$ catalysts. *Catal. Today* **2014**, *228*, 138–144. [CrossRef]
78. Bahari, M.B.; Setiabudi, H.D.; Nishino, T.; Ayas, N.; Vo, D.V.N. Coke-resistant Y_2O_3-promoted cobalt supported on mesoporous alumina for enhanced hydrogen production. *J. Energy Inst.* **2021**, *94*, 272–284. [CrossRef]
79. Taherian, Z.; Gharahshiran, V.S.; Fazlikhani, F.; Yousefpour, M. Catalytic performance of Samarium-modified Ni catalysts over $Al_2O_3–CaO$ support for dry reforming of methane. *Int. J. Hydrogen Energy* **2021**, *46*, 7254–7262. [CrossRef]
80. Zhang, M.; Zhang, J.; Zhou, Z.; Chen, S.; Zhang, T.; Song, F.; Zhang, Q.; Tsubaki, N.; Tan, Y.; Han, Y. Effects of the surface adsorbed oxygen species tuned by rare-earth metal doping on dry reforming of methane over Ni/ZrO_2 catalyst. *Appl. Catal. B Environ.* **2019**, *264*, 118522. [CrossRef]
81. Figueredo, G.P.; Medeiros, R.L.; Macedo, H.P.; de Oliveira, A.; Braga, R.M.; Mercury, J.M.; Melo, M.A.; Melo, D.M. A comparative study of dry reforming of methane over nickel catalysts supported on perovskite-type $LaAlO_3$ and commercial α-Al_2O_3. *Int. J. Hydrogen Energy* **2018**, *43*, 11022–11037. [CrossRef]
82. Tsoukalou, A.; Imtiaz, Q.; Kim, S.M.; Abdala, P.; Yoon, S.; Müller, C.R. Dry-reforming of methane over bimetallic $Ni–M/La_2O_3$ (M = Co, Fe): The effect of the rate of $La_2O_2CO_3$ formation and phase stability on the catalytic activity and stability. *J. Catal.* **2016**, *343*, 208–214. [CrossRef]
83. Suntivich, J.; Gasteiger, H.A.; Yabuuchi, N.; Nakanishi, H.; Goodenough, J.B.; Shao-Horn, Y. Design principles for oxygen-reduction activity on perovskite oxide catalysts for fuel cells and metal–air batteries. *Nat. Chem.* **2011**, *3*, 546–550. [CrossRef]
84. Van der Heide, P.A.W. Systematic x-ray photoelectron spectroscopic study of La1-xSrx-based perovskite-type oxides. *Surf. Interface Anal.* **2002**, *33*, 414–425. [CrossRef]
85. Shahnazi, A.; Firoozi, S. Improving the catalytic performance of $LaNiO_3$ perovskite by manganese substitution via ultrasonic spray pyrolysis for dry reforming of methane. *J. CO2 Util.* **2021**, *45*, 101455. [CrossRef]
86. Kim, H.S.; Jeon, Y.; Kim, J.H.; Jang, G.Y.; Yoon, S.P.; Yun, J.W. Characteristics of $Sr_{1-x}Y_xTi_{1-y}RuyO_{3+/-\delta}$ and Ru-impregnated $Sr_{1-x}Y_xTiO_{3+/-\delta}$ perovskite catalysts as SOFC anode for methane dry reforming. *Appl. Surf. Sci.* **2020**, *510*, 145450. [CrossRef]
87. Yang, E.-H.; Noh, Y.S.; Hong, G.H.; Moon, D.J. Combined steam and CO_2 reforming of methane over $La_{1-x}Sr_xNiO_3$ perovskite oxides. *Catal. Today* **2018**, *299*, 242–250. [CrossRef]
88. Bhattar, S.; Abedin, M.A.; Shekhawat, D.; Haynes, D.J.; Spivey, J.J. The effect of La substitution by Sr- and Ca- in Ni substituted Lanthanum Zirconate pyrochlore catalysts for dry reforming of methane. *Appl. Catal. A Gen.* **2020**, *602*, 117721. [CrossRef]
89. Misture, S.T.; McDevitt, K.M.; Glass, K.C.; Edwards, D.D.; Howe, J.Y.; Rector, K.D.; He, H.; Vogel, S.C. Sulfur-resistant and regenerable Ni/Co spinel-based catalysts for methane dry reforming. *Catal. Sci. Technol.* **2015**, *5*, 4565–4574. [CrossRef]
90. Jiang, C.; Loisel, E.; Cullen, D.A.; Dorman, J.A.; Dooley, K.M. On the enhanced sulfur and coking tolerance of Ni-Co-rare earth oxide catalysts for the dry reforming of methane. *J. Catal.* **2020**, *393*, 215–229. [CrossRef]
91. Khoja, A.H.; Tahir, M.; Amin, N.A.S. Evaluating the performance of Ni catalyst supported on $La_2O_3–MgAl_2O_4$ for dry re-forming of methane in a packed bed dielectric barrier discharge (DBD) plasma reactor. *Energy Fuels* **2019**, *33*, 11630–11647. [CrossRef]
92. Zhang, Z.; Zhao, G.; Bi, G.; Guo, Y.; Xie, J. Monolithic SiC-foam supported $NiLa_2O_3$ composites for dry reforming of methane with enhanced carbon resistance. *Fuel Process. Technol.* **2021**, *212*, 106627. [CrossRef]
93. Cho, E.; Lee, Y.-H.; Kim, H.; Jang, E.J.; Kwak, J.H.; Lee, K.; Ko, C.H.; Yoon, W.L. Ni catalysts for dry methane reforming prepared by A-site exsolution on mesoporous defect spinel magnesium aluminate. *Appl. Catal. A Gen.* **2020**, *602*, 117694. [CrossRef]